ROYAL SOCIETY
OF CHEMISTRY

COMMUNICATION

Check for updates

New lead bromide chiral perovskites with ultra-broadband white-light emission†

Yalan Liu,‡[a] Chao Wang,‡[a] Yurong Guo,[a] Linlin Ma,[a] Chenyang Zhou,[a] Ya Liu,[ab] Lina Zhu,[a] Xiaozeng Li,[a] Mingxing Zhang[ab] and Guangjiu Zhao ⬤ *[a]

Herein, we present for the first time on the synthesis of two chiral perovskites with white-light emission and an achiral perovskite featuring a spectral blueshift. Moreover, the luminescence mechanism of these perovskites is investigated. The direct signals of the free excitons (FEs) and self-trapped excitons (STEs) were observed by performing time-resolved nanosecond transient absorption measurements for our perovskites. This directly verifies that the broad emission indeed originates from FE and STEs. The time-resolved transient emission curves manifest that the long-lived component is assigned to STEs transition and short-lived component is ascribed to FE transition. This study promotes the development of multifunctional applications of chiral white-light emissive perovskites.

Introduction

Organic–inorganic hybrid perovskites have drawn increasing attention for their promising applications in photovoltaic cells, light-emitting diodes (LEDs), photodetectors, and so on.[1–9] Importantly, low-dimensional perovskites have a common broadband emission and large Stokes shifts, which is assigned to the existence of STEs and provides a probability of generating white-light emission.[10–19] A single-component white-light emissive phosphor plays an important role in preparing high-quality white-light-emitting diodes (WLEDs), which is ascribed to resolving two problems of self-absorption and spectral shift.[20–26] Therefore, significant efforts need to be made to obtain single-component white emissive low-dimensional hybrid perovskites.

[a] *Tianjin Key Laboratory of Molecular Optoelectronic Sciences, National Demonstration Center for Experimental Chemistry & Chemical engineering Education, National Virtual Simulation Experimental Teaching Center for Chemistry & Chemical engineering Education, Department of Chemistry, School of Science, Tianjin University, Tianjin 300354, China. E-mail: gjzhao@tju.edu.cn*

[b] *State Key Laboratory of Molecular Reaction Dynamics, Dalian Institute of Chemical Physics, Chinese Academy of Sciences, Dalian 116023, China*

† Electronic supplementary information (ESI) available. See DOI: 10.1039/d0tc00881h

‡ These authors are equally contributed to this work.

Meanwhile, the low-dimensional organic–inorganic hybrid perovskites feature the diversity of available ionic compositions and flexible structure, which makes it possible to achieve different optoelectronic properties *via* incorporating functional organic molecules into these perovskites.[27–30] For example, Billing *et al.* synthesized one-dimensional (1D) chiral perovskites *via* the incorporation of chiral organic small molecules for the first time.[31] Ma *et al.* reported the linear optical properties such as circularly polarized luminescence (CPL), and corresponding detection of chiral 2D perovskites.[32] Xiong *et al.* reported the synthesis and ferroelectricity of a series of chiral perovskites.[33] Current studies focus mostly on the linear optical properties,[34,35] second harmonic generation (SHG),[36–38] and electronic properties, including spintronics[39] and ferroelectricity.[40,41] However, to the best of our knowledge, there are no reports on the photoluminescence mechanism of low-dimensional hybrid perovskites with combined chirality and white-light emission.
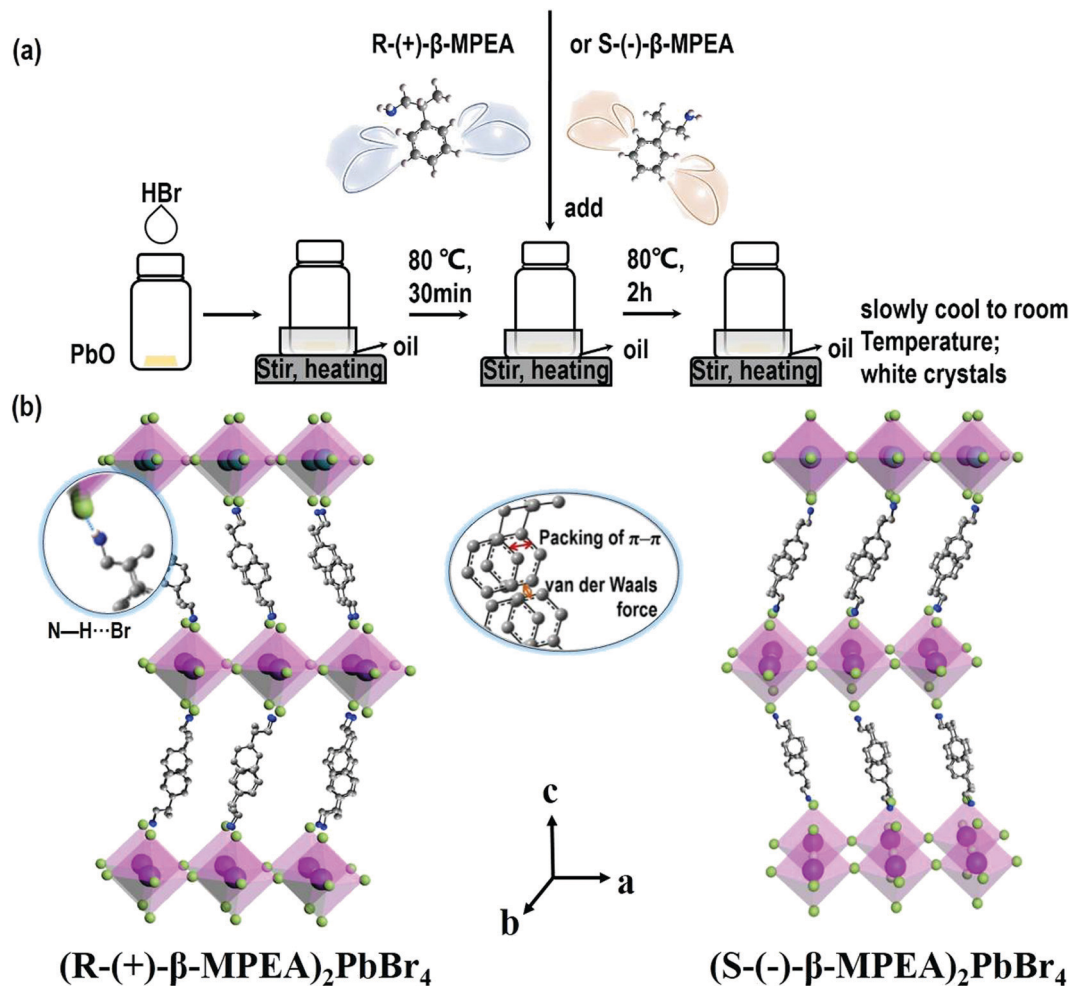
Result and discussion

Here, we first reported the synthesis of chiral 2D perovskites $(R\text{-}(+)\text{-}\beta\text{-MPEA})_2PbBr_4$ and $(S\text{-}(-)\text{-}\beta\text{-MPEA})_2PbBr_4$ (β-MPEA = beta-methylphenethylamine, where *S*- and *R*-MPEA represent the molecules with opposite chirality) with ultra-broadband white-light emission. The schematic experimental operation of chiral perovskites is shown in Scheme 1a. Chiral perovskite crystals are synthesized *via* a solution method using chiral organic ligands, in which chiral cations are rationally introduced to achieve the spatial inversion asymmetry. We also synthesized achiral perovskite crystals $((rac)\text{-MPEA})_2PbBr_4$, (racemic beta-methylphenethylamine) using equal proportions of *R*-(+)- and *S*-(−)-β-MPEA as controls, further details are given in the ESI.† Scheme 1b displays the schematic structural illustration of chiral perovskite crystals. Two layers of chiral molecules sandwich a layer of corner-sharing $[PbBr_6]^{4-}$ octahedral layer. Chiral organic cations in the perovskite crystal are held together by the van der Waals force and were stabilized

This journal is © The Royal Society of Chemistry 2020

J. Mater. Chem. C, 2020, 8, 5673–5680 | **5673**

Scheme 1 (a) The schematic experimental operation diagram. (b) The structural illustration of crystals of (R-(+)-β-and S-(−)-β-MPEA)$_2$PbBr$_4$ (yellow-green ball = bromide atom, sky-blue ball = lead atom, gray ball = carbon atom, deep-blue ball = nitrogen atom, and pink-white ball = hydrogen atom).

here through π–π packing interactions. The inorganic layers and organic cations were connected by the hydrogen bonding of N–H···Br. (R-(+)-β-MPEA)$_2$PbBr$_4$ exhibits a white color and a needle-like shape (Fig. 1a), and emits white-light under the UV light of 365 nm (Fig. 1b). The scanning electron microscopy

(SEM) image of (R-(+)-β-MPEA)$_2$PbBr$_4$ shows that the surface is smooth (Fig. 1c). To confirm the chemical composition of (R-(+)-β-MPEA)$_2$PbBr$_4$, we performed the energy-dispersive X-ray spectroscopy (EDS) measurement. As shown in Fig. S1 (ESI†), the C, N, Pb, and Br elements are distributed through

Fig. 1 The optical image under (a) ambient light and (b) UV light (365 nm), (c) SEM image (scale bar is 5 μm) and element mapping images of (R-(+)-β-MPEA)$_2$PbBr$_4$. (d) The XRD patterns of perovskite crystals.

the selected areas (marked by a square). The presence of the O element is assigned to the preparation in air. $(S-(-)-\beta-$MPEA$)_2$PbBr$_4$ and $((rac)$-MPEA$)_2$PbBr$_4$ have similar properties (Fig. S2 and S3, ESI†). The X-ray diffraction (XRD) patterns of these as-synthesized perovskites exhibit sharp peaks with narrow full-width at half-maximum values, which further indicate that all of our perovskites have good crystallinity (Fig. 1d). We further investigated the thermal stability of these perovskite crystals. As shown in Fig. S4 (ESI†), the thermal gravimetric analysis (TGA) measurements reveal that our perovskite crystals exhibit thermal stability up to a decomposition temperature of approximately 220 °C.

To confirm the chirality of our perovskite crystals, we further carried out circular dichroism (CD). We measured CD using thin-films of these perovskites. Scheme S1 (ESI†) represents a spin-coating method to prepare thin-films. The as-formed perovskite crystals were spin-coated at 2000 rpm for 30 s on a clean quartz glass substrate with a 250 mg ml^{-1} precursor

solution in dimethylformamide (DMF). After a heat treatment at 65 °C for 2 min, thin-films were formed (see the methods in the ESI†). The X-ray diffraction (XRD) patterns of the as-formed perovskite crystal thin-films are shown in Fig. 2a and Fig. S5 (ESI†). For comparison, the characteristic peak of the thin films appeared due to successful preparation. When the CD of the thin films was measured, $(R-(+)-\beta$-MPEA$)_2$PbBr$_4$ and $(S-(-)-\beta-$MPEA$)_2$PbBr$_4$ were found to have evident CD signals, while $((rac)$-MPEA$)_2$PbBr$_4$ displayed a featureless flat signal (Fig. 3b). The peaks in the CD spectra of $(R-(+)-\beta$-MPEA$)_2$PbBr$_4$ and $(S-(-)-\beta$-MPEA$)_2$PbBr$_4$ are observed at the same position at 289 nm, 321 nm, 388 nm, and 398 nm. However, the peaks of $(R-(+)-\beta$-MPEA$)_2$PbBr$_4$ and $(S-(-)-\beta$-MPEA$)_2$PbBr$_4$ have opposite signs, as shown in Fig. 2b. The presence of the oppositely signed CD in $(R-(+)-\beta$-MPEA$)_2$PbBr$_4$ and $(S-(-)-\beta$-MPEA$)_2$PbBr$_4$ confirms that the incorporation of the chiral organic molecules can successfully endow perovskites with chirality. In detail, $(R-(+)-\beta$-MPEA$)_2$PbBr$_4$ and $(S-(-)-\beta$-MPEA$)_2$PbBr$_4$ do not show
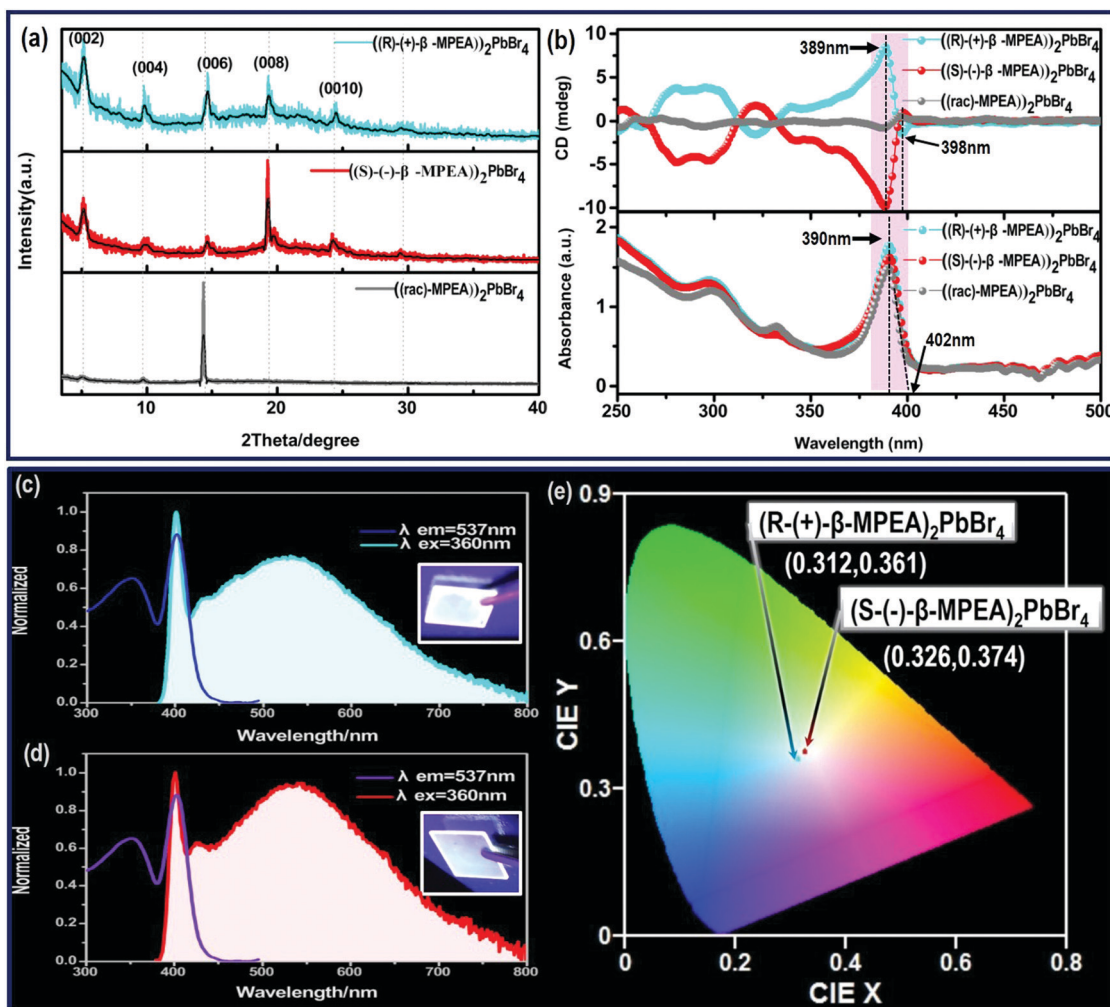

Fig. 2 (a) The XRD patterns of chiral perovskite crystals $(R-(+)-\beta$-and $S-(-)-\beta$-MPEA$)_2$PbBr$_4$, $(rac$-MPEA$)_2$PbBr$_4$ film, (b) circular dichroism and steady-state absorption spectra of these perovskite crystals film. (c) PL and PLE spectra of $(R-(+)-\beta$-MPEA$)_2$PbBr$_4$ and $(S-(-)-\beta$-MPEA$)_2$PbBr$_4$ film (λ_{ex} = 360 nm, λ_{em} = 537 nm), (d) PL and PLE spectra of $(S-(-)-\beta$-MPEA$)_2$PbBr$_4$ and $(S-(-)-\beta$-MPEA$)_2$PbBr$_4$ film (λ_{ex} = 360 nm, λ_{em} = 537 nm), (e) CIE coordinated of the emissions of $(R-(+)-\beta$-MPEA$)_2$PbBr$_4$ and $(S-(-)-\beta$-MPEA$)_2$PbBr$_4$ film.

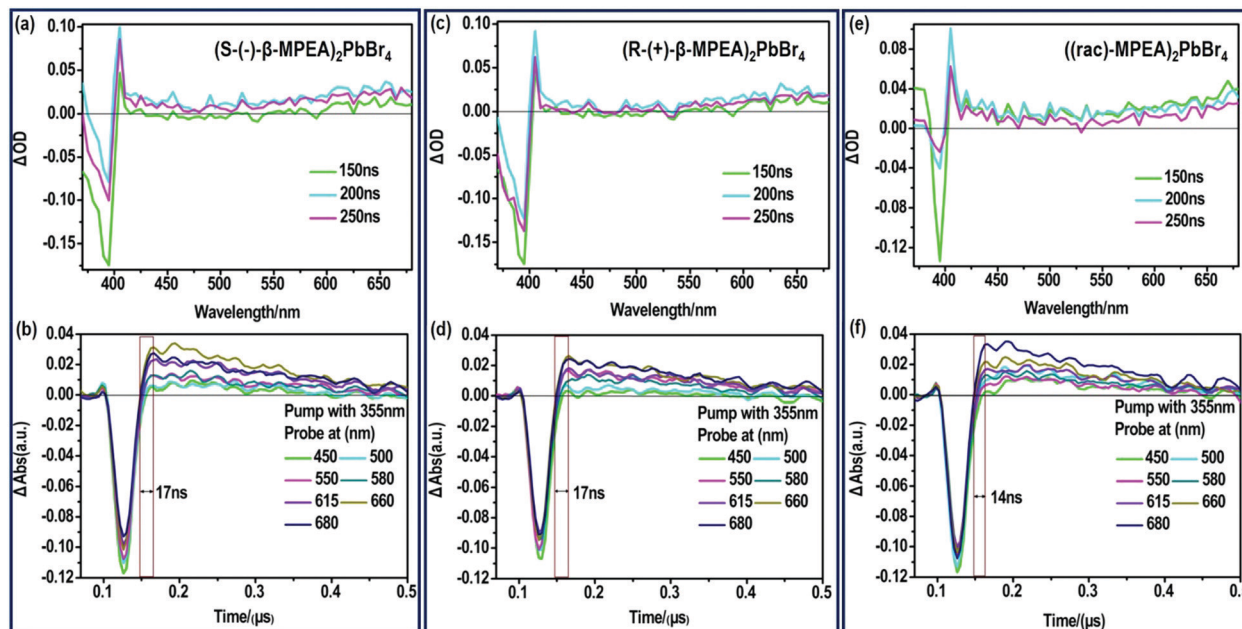This journal is © The Royal Society of Chemistry 2020

J. Mater. Chem. C, 2020, **8**, 5673–5680 | **5675**

Fig. 3 ns-TA spectra of (a) (S-β-MPEA)$_2$PbBr$_4$, (c) (R-β-MPEA)$_2$PbBr$_4$, (e) ((rac)-MPEA)$_2$PbBr$_4$ films upon excitation at 355 nm. TA onsets of (b) (S-β-MPEA)$_2$PbBr$_4$ (d) (R-β-MPEA)$_2$PbBr$_4$, (f) ((rac)-MPEA)$_2$PbBr$_4$ films probed at different wavelength.

absolutely mirror-imaged CD signals with a weak dissymmetry factor. A comparison of the CD spectra and absorption spectra of the chiral films reveal that the CD peaks are located before the absorption band edge. The peak observed at 390 nm was extrapolated to 402 nm. It is found that the CD signal of (R-(+)-β-MPEA)$_2$PbBr$_4$ and (S-(−)-β-MPEA)$_2$PbBr$_4$ change the sign close to the absorption band edge. This phenomenon can be interpreted as the Cotton effect.[42] Furthermore, the observed CD could be ascribed to the transition of electrons in the electronic bands, which in turn supported the observed Cotton effect. In addition, the changes in the CD signal in the wavelength region ranging from 250 to 325 nm can be attributed to additional excitonic transitions, whereas the CD signal in the longer wavelength region of the band edge actually originates from circular differential scattering according to the previous report.[35] All of these findings support that chirality has been transferred from the solely organic cations to the overall (R-(+)-β-MPEA)2PbBr$_4$ or (S-(−)-β-MPEA)$_2$PbBr$_4$ perovskite crystals, while chirality exists only in organic cations for ((rac)-MPEA)$_2$PbBr$_4$ perovskite crystals. These results contribute to further optical properties of chiral and achiral perovskites.

Next, the photophysical properties of the perovskite system were measured via photoluminescence excitation (PLE) and PL emission spectra. As shown in Fig. 2c and d, (R-(+)-β-MPEA)$_2$PbBr$_4$ and (S-(−)-β-MPEA)$_2$PbBr$_4$ both exhibit ultra-broadband emission spectrum ranging from 385 nm to 800 nm, and two emission peaks: a narrow emission located at 402 nm and a broad emission centered at 535 nm with an excitation wavelength of 360 nm. The origin of the unusual dual-peak emission is ascribed to free exciton (FE) and self-trapped exciton (STE) recombination, which will be discussed in detail in the later analysis of the ultra-fast spectra. Compared with (R-(+)-β-MPEA)$_2$PbBr$_4$,

the intensity of the 402 nm emission of (S-(−)-β-MPEA)$_2$PbBr$_4$ remains unchanged, while the intensity of the 537 nm emission of (S-(−)-β-MPEA)$_2$PbBr$_4$ increased. Therefore, (R-(+)-β-MPEA)$_2$PbBr$_4$ and (S-(−)-β-MPEA)$_2$PbBr$_4$ perovskite exhibit white-light emissions with the CIE chromaticity coordinates of (0.312, 0.361) and (0.326, 0.374), respectively, as shown in Fig. 2e. Meanwhile, both chiral perovskite films could emit white-light under UV light photoexcitation of 365 nm, as shown in Fig. 2a and b inset. Two chiral perovskites have a photoluminescence quantum yield (PLQY) of approximately 1%. According to the previous reports,[43–45] the low-dimensional perovskites, particularly 1D or 2D perovskites emitting from both FE and STE excited state, rarely achieve high PLQY due to electronic band formation and aggregation-induced self-quenching in the solid-state. It is not difficult to understand that two chiral perovskites have a low PLQY. In addition, the PL spectrum of (rac-MPEA)$_2$PbBr$_4$ perovskite exhibits a non-Gaussian distribution emission located at 408 nm, as shown in Fig. S6 (ESI†). Compared with chiral perovskites, ((rac)-MPEA)$_2$PbBr$_4$ emits much stronger light with CIE chromaticity coordinates of (0.260, 0.290) and has a much higher PLQY of 5%. Therefore, the difference between R- and S-configure chiral cations may change the weak interactions existing in the perovskite crystal structure such as the hydrogen bonding and van der Waals force, which results in the optical difference, as shown in the CIE chromaticity coordinate and PLQY. Table S1 (ESI†) lists some reported PLQY and CIE chromaticity coordinates for white-light-emitting perovskites. Through comparison, the PLQY for our white-light-emitting perovskites is comparable and not particularly low. Besides, the presence of the same PbBr$_4$$^{2−}$ frameworks and cross-sectional aromatic area indicates a similar structure and is further attributed to optical similarity, as shown in the absorption spectra.

5676 | J. Mater. Chem. C, 2020, 8, 5673–5680

This journal is © The Royal Society of Chemistry 2020

To further verify that the ultra-broadband emission of the perovskites originates from FE and STE, we subsequently performed nanosecond time-resolved transient absorption (ns-TA) spectroscopy to directly observe the signal of FE and STE, as presented in Fig. 3. The ns-TA spectra of $(S-(-)-\beta$-MPEA$)_2$PbBr$_4$, $(R-(+)-\beta$-MPEA$)_2$PbBr$_4$, and $((rac)$-MPEA$)_2$PbBr$_4$ are shown in Fig. 3a, b, c, d, e and f, respectively. The ns-TA spectroscopy was carried out by conforming to the above-excitonic-peak excitation at 355 nm with pulse energy of 7 mJ. The characteristic bleach peak of 395 nm and a remarkable broad absorption with energy below that of excitons are observed in Fig. 4a–c, which support that the emission of our perovskites originates from FE and STE. The same position of the bleach peak exhibits similar exciton absorption for these perovskites, which is assigned to the presence of the same PbBr$_4{}^{2-}$ frameworks. In addition, it is reported that the formation time of STE demonstrates itself in the rise time of the observed induced absorption.[10,12,46–50] The formation time of STE in $(rac$-MPEA$)_2$PbBr$_4$ is shorter than that of two chiral perovskites (Fig. 3b, d and f), which show a low potential barrier between the FE and STE states for $((rac)$-MPEA$)_2$PbBr$_4$. $(S-(-)-\beta$-MPEA$)_2$PbBr$_4$ and $(R-(+)-\beta$-MPEA$)_2$PbBr$_4$ have the same formation time of STE, which indicates that there was no difference in the potential energy barrier between the FE and STE states for the two perovskites. To further comprehend the photoluminescence mechanism, we performed a Gaussian curve fitting and nanosecond time-resolved PL emission (ns-TE) spectroscopy.

The ns-TE spectra and Gaussian curve fitting of the PL spectra of these perovskites are shown in Fig. S6, ESI† and Fig. 4. These Gaussian peaks were found to give the optimal fit to the corresponding spectrum in Fig. S7a (ESI†). Compared with the chiral perovskites, the distribution of high-energy peaks increased for $((rac)$-MPEA$)_2$PbBr$_4$. We assume that the self-depth of $((rac)$-MPEA$)_2$PbBr$_4$ may be smaller than chiral perovskites. The comparison of ns-TE with the corresponding reverse-normalized PL spectra of three perovskites is shown in Fig. S7b–d (ESI†). The distribution of high-energy peaks in $((rac)$-MPEA$)_2$PbBr$_4$ increases, while the distribution of low-energy peaks decreases, in accordance with the Gaussian curve fitting analysis. This further supports the previous assumption for the self-trapped depth. Another remarkable observation is that there is a common maximum emission peak at 435 nm. For all three perovskites, the PL decay monitored at 435 nm can be satisfactorily fitted with a biexponential decay (Fig. 4). The fast decay process (τ_1) corresponds to the FE transition, while the slower decay process (τ_2) is assigned to the STE transition. More explicitly, for $(S-(-)-\beta$-MPEA$)_2$PbBr$_4$, a biexponential decay has a 16 ns component (92%) and a 120 ns component (8%) in Fig. 4a. For $(R-(+)-\beta$-MPEA$)_2$PbBr$_4$, a biexponential decay has a 19.5 ns component (95%) and a 108 ns component (5%) in Fig. 4b. For $((rac)$-MPEA$)_2$PbBr$_4$, a biexponential decay has a 60.1 ns component (62%) and a 351 ns component (38%) in Fig. 4c. The proportion of the STE component for $(R-(+)-\beta$-MPEA$)_2$PbBr$_4$ decrease in contrast to that of $(S-(-)-\beta$-MPEA$)_2$PbBr$_4$. The ns-TA data analysis shows the same potential barrier between
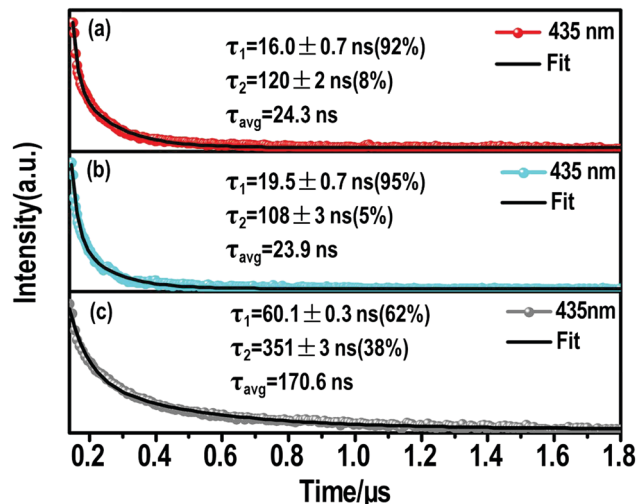

Fig. 4 Nanosecond time-resolve emission (ns-TE) decays and fittings of the (a) $(S-\beta$-MPEA$)_2$PbBr$_4$, (b) $(R-\beta$-MPEA$)_2$PbBr$_4$, and (c) $((rac)$-MPEA$)_2$PbBr$_4$ emission at 435 nm.

FE and STE for $(R-(+)-\beta$-MPEA$)_2$PbBr$_4$ and $(S-(-)-\beta$-MPEA$)_2$PbBr$_4$. Both results manifest that some different defects tune radiative or nonradiative transitions and further change luminescence. Some defects that promote nonradiative transition between STE and ground state (GS) existed in $(R-(+)-\beta$-MPEA$)_2$PbBr$_4$, which is consistent with the decrease in the long-lived STE emission component. In addition, the significant increase in the long-lived component proportion for $((rac)$-MPEA$)_2$PbBr$_4$ suggests that the transition from STEs to FEs has a low potential energy barrier, and more FEs were trapped to generate STEs, in accordance with the result of the ns-TA measurement. According to the previous reports,[51,52] the inorganic and two kinds of chiral organic components couple to electronic subsystem and induce much rapid coherence loss for $((rac)$-MPEA$)_2$PbBr$_4$. The rapid loss of coherence also explains the significant increase in the long-lived component proportions. Meanwhile, the PLQY of $((rac)$-MPEA$)_2$PbBr$_4$ was much higher than that of chiral perovskites, which is ascribed to the removal of some defects that are in favor of nonradiative transition.

The photophysical mechanism of the ultra-broadband emission in the perovskite systems can be depicted, as shown in Fig. 5, based on the above discussions. Detail follows: upon photoexcitation, electrons in the GS were motivated to the FE state for the chiral perovskite systems. Some FEs can return to GS via radiative or nonradiative transition forms directly. Some FEs were trapped by the STE states to further produce the STE emission or non-radiative transition. Some FEs trapped by the STE states undergo back energy transfer to return to the FE state first, and then return to GS after emitting light. All the transitions happened in the chiral system simultaneously. The presence of chirality can generate some defects, which is in favor of nonradiative transitions (particularly STE nonradiative transition). It is not difficult to understand that the chiral perovskites have a PLQY of approximately 1% and lack a long-lived component. Compared with the chiral perovskites,
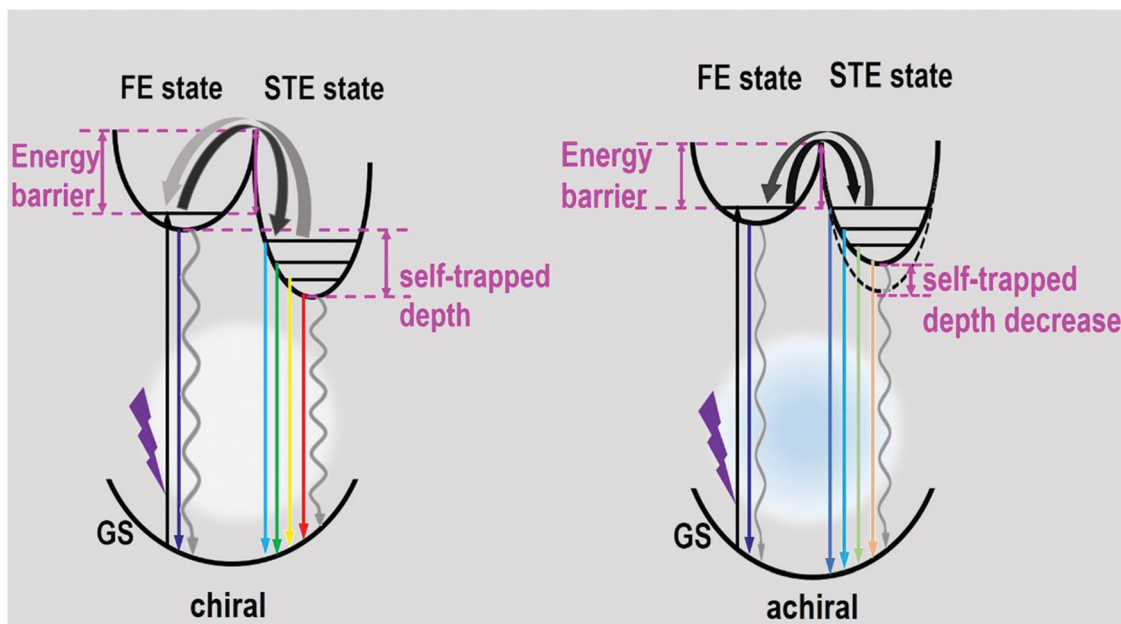
This journal is © The Royal Society of Chemistry 2020

J. Mater. Chem. C, 2020, **8**, 5673–5680 | **5677**

Fig. 5 Diagram of luminescence processes in the as-formed perovskite crystals. (GS: ground state, FE state: free-exciton state, STE state: self-trapped exciton state.)

the achiral perovskite has a low energy barrier between FE and STE and a higher proportion of the long-lived components, both manifesting that the transitions between the FE state and STE state are not restricted. The luminescence of achiral perovskite exhibits a blueshift. Moreover, the high energy emission peaks of the achiral perovskite increased. Both of them indicate that the self-trapped depth of the achiral perovskite was smaller than that of chiral perovskites, as shown in Fig. 5. In addition, the disappearance of chirality may remove some defects, which promotes the radiative transition. These all support that the PLQY of the achiral perovskite was much higher than that of two chiral perovskites. Finally, the ultra-broadband emission of our perovskites indeed originates from FE and STE.

Conclusions

In summary, we synthesized two chiral perovskites with broadband white-light emission and a remarkable CD signal, and an achiral perovskite ((*rac*)-MPEA)$_2$PbBr$_4$ with a featureless flat CD signal and spectral slight blue shift. The difference between *R*- and *S*-configure chiral cations may change the weak interaction existing in the perovskite crystal structure, which results in the optical difference, as shown in the luminescence and PLQY. In addition, the presence of the same PbBr$_4^{2-}$ frameworks and cross-sectional aromatic area suggests a similar structure and is further attributed to optical similarity, as shown in the absorption spectra. Moreover, the overall photoluminescence mechanism of these perovskites was formulated by a comprehensive analysis of the steady-state spectra and ultra-fast spectra. The direct signal of FE and STE was observed in the ns-TA spectra, which verifies that the ultra-broadband emission of our perovskites indeed originated from FE and STE. Meanwhile, the

ns-TA spectra show that the formation time of STE in the achiral perovskite was shorter than that of chiral perovskites, which reveals a low potential barrier between the FE and STE states and the decrease in the self-trapped depth in the achiral perovskite. The ns-TE curves further manifest that the long-lived component is assigned to the STE transition, and the short-lived component is ascribed to the FE transition. These all support our luminescence mechanism. Thus, this study not only provides a new design by combining white-light emission and chirality but also promotes the development of the multifunctional application of white-light emissive perovskite materials.

Conflicts of interest

There are no conflicts to declare.

Acknowledgements

Notes and references

1 A. Kojima, K. Teshima, Y. Shirai and T. Miyasaka, *J. Am. Chem. Soc.*, 2009, **131**, 6050–6051.

2 M. M. Lee, J. Teuscher, T. Miyasaka, T. N. Murakami and H. J. Snaith, *Science*, 2012, **338**, 643–647.

3 S. T. Ha, X. Liu, Q. Zhang, D. Giovanni, T. C. Sum and Q. Xiong, *Adv. Opt. Mater.*, 2017, **2**, 838–844.

4 F. Zhang, H. Zhong, C. Chen, X.-g. Wu, X. Hu, H. Huang, J. Han, B. Zou and Y. Dong, *ACS Nano*, 2015, **9**, 4533–4542.

5 N. Wang, L. Cheng, R. Ge, S. Zhang, Y. Miao, W. Zou, C. Yi, Y. Sun, Y. Cao, R. Yang, Y. Q. Wei, Q. Guo, Y. Ke., M. T. Yu, Y. Z. Jin, Y. Liu, Q. Q. Ding, D. W. Di, L. Yang, G. C. Xing, H. Tian, C. H. Jin, F. Gao, R. H. Friend, J. P. Wang and W. Huang, *Nat. Photonics*, 2016, **10**, 699–704.

6 H. L. Wang, F. Yang, Y. R. Xiang, S. A. Ye, X. Peng, J. Song, J. L. Qu and W. Y. Wong, *J. Mater. Chem. A*, 2019, **7**, 24191–24198.

7 B. Yang, J. S. Chen, Q. Shi, Z. J. Wang, M. Gerhard, A. Dobrovolsky, I. G. Scheblykin, K. J. Karki and K. L. Han, *J. Phys. Chem. Lett.*, 2018, **8**, 5017–5022.

8 Y. Cheng, Z. F. Shi, S. T. Yin, S. li, S. Li, W. Q. Liang, D. Wu, Y. T. Tian and X. J. Li, *Sol. Energy Mater. Sol. Cells*, 2020, **204**, 110230.

9 A. Abate, M. Planells, D. J. Hollman, V. Barthi, S. Chand, H. J. Snaith and N. Robertson, *Phys. Chem. Chem. Phys.*, 2015, **17**, 2335–2338.

10 Y. Li, Z. F. Shi, L. Z. Lei, S. Li, D. W. Yang, T. T. Xu, Y. Z. Tian, Y. G. Lu, Y. Wang, L. J. Zhang, X. J. Li, Y. T. Zhang, G. T. Du and C. X. Shan, *Adv. Mater. Interfaces*, 2019, **6**, 1900188.

11 Z. Z. Ma, Z. F. Shi, C. C. Qin, M. H. Cui, D. W. Yang, X. J. Wang, L. T. Wang, X. Z. Ji, J. L. Sun, D. Wu, Y. Zhang, X. J. Li, L. J. Zhang and C. X. Shan, *ACS Nano*, 2020, DOI: 10.1021/acsnano.9b10148.

12 T. Hu, M. D. Smith, E. R. Dohner, M. J. Sher, X. Wu, M. T. Trinh, A. Fisher, J. Corbett, X. Y. Zhu, H. I. Karunadasa and A. M. Lindenberg, *J. Phys. Chem. Lett.*, 2016, **7**, 2258–2263.

13 M. G. Ju, J. Dai, L. Ma, Y. Y. Zhou and X. C. Zeng, *J. Am. Chem. Soc.*, 2018, **140**, 10456–10463.

14 M. D. Smith and H. I. Karunadasa, *Acc. Chem. Res.*, 2018, **51**, 619–627.

15 Z. Yuan, C. K. Zhou, Y. Tian, Y. Shu, J. Messier, J. C. Wang, L. J. van de Burgt, K. Kountouriotis, Y. Xin, E. Holt, K. Schanze, R. Clark, T. Siegrist and B. W. Ma, *Nat. Commun.*, 2017, **8**, 14051.

16 R. T. Williams and K. S. Song, *J. Phys. Chem. Solids*, 1990, **51**, 679–716.

17 L. L. Mao, P. J. Guo, M. Kepenekian, I. Hadar, C. Katan, J. Even, R. D. Schaller, C. C. Stoumpos and M. G. Kanatzidis, *J. Am. Chem. Soc.*, 2018, **140**, 13078–13088.

18 K. M. Mccall, C. C. Stoumpos, S. S. Kostina, M. G. Kanatzidis and B. W. Wessels, *Chem. Mater.*, 2017, **29**, 4129–4145.

19 Y. L. Liu, C. Wang, C. Y. Zhou, P. Li, L. N. Zhu, S. Q. Sun, X. Feng, Y. Sun and G. J. Zhao, *J. Lumin.*, 2020, **221**, 117045.

20 J. S. Kim, P. E. Jeon, Y. H. Park, J. C. Choi, H. L. Park, G. C. Kim and T. W. Kim, *Appl. Phys. Lett.*, 2004, **85**, 3696–3698.

21 C. C. Lin and R.-S. Liu, *J. Phys. Chem. Lett.*, 2011, **2**, 1268–1277.

22 Q.-Y. Yang and J.-M. Lehn, *Angew. Chem., Int. Ed.*, 2014, **53**, 4572–4577.

23 Z. Xie, C. Chen, S. Xu, J. Li, Y. Zhang, S. Liu, J. Xu and Z. Chi, *Angew. Chem., Int. Ed.*, 2015, **54**, 7181–7184.

24 Z. Yuan, C. Zhou, J. Messier, Y. Tian, Y. Shu, J. Wang, Y. Xin and B. W. Ma, *Adv. Opt. Mater.*, 2016, **4**, 2009–2015.

25 J. Luo, X. Wang, S. Li, J. Liu, Y. Guo, G. Niu, L. Yao, Y. Fu, L. Gao and Q. Dong, *Nature*, 2018, **563**, 541.

26 S. Yang, Z. Lin, J. Wang, Y. Chen, Z. Liu, E. Yang, J. Zhang and Q. Ling, *ACS Appl. Mater. Interfaces*, 2018, **10**, 15980–15987.

27 D. B. Mitzi, *J. Chem. Soc., Dalton Trans.*, 2001, **1**, 1–12.

28 Y. Zhou, Z. J. Yong, K. C. Zhang, B. M. Liu, Z. W. Wang, J. S. Hou, Y. Z. Fang, Y. Zhou, H. T. Sun and B. Song, *J. Phys. Chem. Lett.*, 2016, **7**, 2735–2741.

29 C. M. Weidman, M. Seitz, S. D. Stranks and W. A. Tisdale, *ACS Nano*, 2016, **10**, 7830–7839.

30 W. Li, Z. Wang, F. Deschler, S. Gao, R. H. Friend and A. K. Cheetham, *Nat. Rev. Mater.*, 2017, **2**, 16099.

31 D. G. Billing and A. Lemmerer, *CrystEngComm*, 2006, **8**, 686–695.

32 J. Ma, C. Fang, C. Chen, L. Jin, J. Wang, S. Wang, J. Tang and D. H. Li, *ACS Nano*, 2019, **13**, 3659–3665.

33 H.-Y. Ye, Y.-Y. Tang, P.-F. Li, W.-Q. Liao, J.-X. Gao, X.-N. Hua, H. Cai, P.-P. Shi, Y.-M. You and R.-G. Xiong, *Science*, 2018, **361**, 151–155.

34 W. J. Chen, S. Zhang, M. H. Zhou, T. H. Zhao, X. J. Qin, X. F. Liu, M. H. Liu and P. F. Duan, *J. Phys. Chem. Lett.*, 2019, **10**, 3290–3295.

35 J. Ahn, E. Lee, J. Tan, W. Yang, B. Kim and J. Moon, *Mater. Horiz.*, 2017, **4**, 851–856.

36 Y. Peng, Y. P. Yao, L. N. Li, Z. Y. Wu, S. S. Wang and J. H. Luo, *J. Mater. Chem. C*, 2018, **6**, 6033–6037.

37 J. Wang, Y. Mi, X. Gao, J. Z. Li, S. G. Lan, C. Fang, H. Z. Shen, X. L. Wen, R. Chen, X. F. Liu, T. C. He and D. H. Li, *Adv. Opt. Mater.*, 2019, 1900398.

38 C. Yuan, X. Li, S. Semin, Y. Feng, T. Rasing and J. Xu, *Nano Lett.*, 2018, **18**, 5411–5417.

39 G. Long, C. Jiang, R. Sabatini, Z. Yang, M. Wei, L. N. Quan, Q. Liang, A. Rasmita, M. Askerka, G. Walters, X. Gong, J. Xing, X. Wen, R. Quintero-Bermudez, H. Yuan, G. Xing, X. R. Wang, D. Song, O. Voznyy, M. Zhang, S. Hoogland, W. Gao, Q. Xiong and E. H. Sargent, *Nat. Photonics*, 2018, **12**, 528–533.

40 C.-K. Yang, W.-N. Chen, Y.-T. Ding, J. Wang, W.-Q. Liao, Y.-Y. Tang, P.-F. Li, Z.-X. Wang and R.-G. Xiong, *Adv. Mater.*, 2019, **31**, 1808088.

41 Y. Ai, X.-G. Chen, P.-P. Shi, Y.-Y. Tang, P.-F. Li, W.-Q. Liao and R.-G. Xiong, *J. Am. Chem. Soc.*, 2019, **141**, 4474–4479.

42 C. Janiak, *J. Chem. Soc., Dalton Trans.*, 2000, **21**, 3885–3896.

43 W. W. Meng, X. M. Wang, Z. W. Xiao, J. B. Wang, D. B. Mitzi and Y. F. Yan, *J. Phys. Chem. Lett.*, 2017, **8**, 2999–3007.

44 J. J. Luo, S. R. Li, H. D. Wu, Y. Zhou, Y. Li, J. Li, J. Liu, J. H. Li, K. H. Li, F. Yi, G. D. Niu and J. Tang, *ACS Photonics*, 2018, **5**, 398–405.

45 J. J. Luo, X. M. Wang, S. R. Li, J. Liu, Y. M. Guo, G. D. Niu, L. Yao, Y. H. Fu, L. Gao, Q. S. Dong, C. Y. Zhao, M. Y. Leng, F. S. Ma, W. X. Liang, L. D. Wang, S. Y. Jin, J. B. Han,

L. J. Zhang, J. Etheridge, J. B. Wang, Y. F. Yan, E. H. Sargent and J. Tang, *Nature*, 2018, 563.

46 A. Ben-Moshe, A. Teitelboim, D. Oron and G. Markovich, *Nano Lett.*, 2016, **16**, 7467–7473.

47 R. L. Zhang, X. Mao, Y. Yang, S. Q. Yang, W. Y. Zhao, T. Wumaier, D. H. Wei, W. Q. Deng and K. L. Han, *Angew. Chem., Int. Ed.*, 2019, **58**, 2725–2729.

48 Y. Peng, L. N. Li, C. M. Ji, Z. Y. Wu, S. S. Wang, X. T. Liu, Y. P. Yao and J. H. Luo, *J. Am. Chem. Soc.*, 2019, **141**, 12197–12201.

49 C. Wang, Y. Liu, X. Feng, C. Y. Zhou, Y. L. Liu and G. J. Zhao, *Angew. Chem., Int. Ed.*, 2019, **58**, 11642–11646.

50 M. Z. Li, J. Zhou, G. J. Zhou, M. S. Molokeev, J. Zhao, V. Morad, M. V. Kovaleko and Z. G. Xia, *Angew. Chem., Int. Ed.*, 2019, **58**, 18670–18675.

51 Z. S. Zhang, W. H. Fang, M. V. Tokina, R. Long and O. V. Prezhdo, *Nano Lett.*, 2018, **18**, 2459–2466.

52 L. Liu, W.-H. Fang, R. Long and O. V. Prezhdo, *J. Phys. Chem. Lett.*, 2018, **9**, 1164–1171.